

Article

Intra-Layer Inhomogeneity of the Anode in Commercial Li-Ion Batteries

Tuo Fang ¹, Guangsen Jiang ², Yong Xia ¹ and Pengfei Ying ^{1,*} 

¹ School of Vehicle and Mobility, Tsinghua University, Beijing 100084, China; ft22@mails.tsinghua.edu.cn (T.F.); xiaiyong@tsinghua.edu.cn (Y.X.)

² Beijing Chehejia Automobile Technology Co., Ltd., Beijing 101399, China; jiangguangsen@lixiang.com

* Correspondence: ypf21@mails.tsinghua.edu.cn

Abstract: The Li intercalation reaction exhibits non-uniform behavior along the thickness direction of the electrode in a Li-ion battery. This non-uniformity, or intra-layer inhomogeneity (ILIH), becomes more serious as the charging and discharging speed increases. Substantial ILIH can lead to Li plating and the emergence of inhomogeneous inner stress, resulting in a decrease in battery service life and an increase in battery safety risks. In this study, an operando optical observation was conducted based on the color change reaction during Li intercalation in the anode. Subsequently, we introduce a novel quantitative method to assess ILIH in commercial Li-ion batteries. A specific ILIH value (K_{ILIH}) is first used in this article for ILIH characterization. An analysis of K_{ILIH} at different charging and discharging rates was conducted, alongside the exploration of K_{ILIH} -SOC trends and their underlying mechanisms. The proposed method exhibits favorable mathematical convergence and physical interpretability, as supported by the results and mechanism analysis. By enabling the assessment of ILIH evolution in response to SOC and (dis)charging rate variations, the proposed method holds significant potential for optimizing fast charging protocols in commercial batteries and contributing to the development of refined electrochemical battery models in future research.

Keywords: Li-ion battery; electric vehicle; battery safety; inhomogeneity; operando observation



Citation: Fang, T.; Jiang, G.; Xia, Y.; Ying, P. Intra-Layer Inhomogeneity of the Anode in Commercial Li-Ion Batteries. *Batteries* **2023**, *9*, 463. <https://doi.org/10.3390/batteries9090463>

Academic Editor: Carlos Ziebert

Received: 18 July 2023

Revised: 8 September 2023

Accepted: 9 September 2023

Published: 12 September 2023



Copyright: © 2023 by the authors. Licensee MDPI, Basel, Switzerland. This article is an open access article distributed under the terms and conditions of the Creative Commons Attribution (CC BY) license (<https://creativecommons.org/licenses/by/4.0/>).

1. Introduction

Lithium-ion batteries (LIBs) have already become the dominant power source for consumer electric devices [1–3]. Since the widespread use of LIBs in electric vehicles (EVs), the ever-increasing market has led to even higher demands for commercial LIBs. To address the requirements of the automobile industry and to alleviate “drive-range anxiety” among consumers, extensive efforts have been made to research and develop LIBs with higher energy density and higher charging rates [4,5]. Other efforts have also been made in the pursuit of LIBs with better cycling performance, higher thermal stability, better safety, and reduced cost [2,6,7].

In the study of LIBs, the potential for fast charging is limited by issues such as reaction inhomogeneity and Li plating. Graphite is commonly used in commercial battery anodes due to its low cost, high Li diffusivity, and low delithiation potential characteristics, but the low-voltage plateau in the charge–discharge profiles of graphite may inevitably increase the risk of Li plating during the fast charging process [8,9]. Li plating and the localized abuse caused by inhomogeneity are recognized as crucial factors leading to reduced lifetime and increased safety risks under abusive operating conditions [10–14]. For example, inhomogeneity-induced local overuse and overcharge can result in internal short circuits under mechanical load, potentially culminating in thermal runaways.

The inhomogeneity of reactions in commercial LIBs can be categorized into three types: in-plane, which refers to inhomogeneity on the surface parallel to the current collector; inter-layer, which represents the variation among electrode layers in full cells; and intra-layer, which describes the inhomogeneity along the thickness direction of the

electrode coating. Numerous studies have investigated inhomogeneity in the in-plane directions [15–18] and the inter-layer dimension [19–21]. However, limited attention has been given to inhomogeneity in the intra-layer direction [11]. Figure 1 shows typical cathode and anode configurations in commercial LIBs, in which the vertical direction of the SEM images and the schematic diagram represents the intra-layer direction mentioned above. Previous studies by Harris et al. [22], Hogrefe et al. [23], and Kuwabara et al. [24] have examined microscopic electrochemical behaviors, the dendrite growth of deposited Li, and contaminated Cu on the cross-section of LIBs, respectively. Although these studies have demonstrated the significance of intra-layer inhomogeneity (ILIH in short), more complex experimental methods, such as operando or in situ techniques, are required for the detailed and quantitative characterization of ILIH.

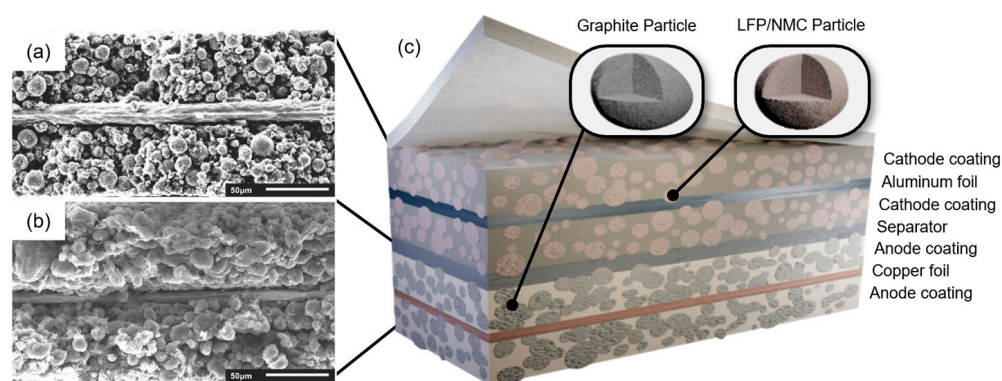


Figure 1. SEM images and a schematic illustration of the electrode structure of LIBs: (a,b) the SEM images of the cross-sections of the cathode and anode in LIBs [25]; and (c) schematic diagram of the electrode structure of LIBs [26].

Compared to ex situ observation and characterization techniques, in situ techniques provide a precise and reliable analysis of battery cells under different conditions (SOCs, etc.). Furthermore, operando techniques make it even more possible to observe and detect batteries during the charging and discharging processes [27]. Consequently, operando or in situ techniques have emerged as a research hotspot in LIBs since the 2010s [28].

Researchers have employed operando or in situ techniques to conduct numerous studies, including investigating Li dendrite growth [29], observing cracks on electrode particles [30], and characterizing Li concentration and current densities in electrodes or electrolytes [31–33], etc. However, there is a relative scarcity of studies focusing on the cross-section of batteries, which require operando techniques and transverse-type samples [28]. Most existing studies have only concentrated on the observation of Li plating and Li dendrite growth [22,29,31,34]. Although Li plating is crucial for studying battery failure, inhomogeneity may be more important for maintaining battery durability from an integrity perspective [10].

To investigate inhomogeneity via the operando approach, optical characterization methods have been developed. For instance, Marie et al. employed an “in situ colorimetry method”, utilizing optical observation to quantify the SOC or potential of graphite electrodes [18,35]. Hogrefe et al. adopted the method to estimate the speed of lithiation by analyzing the colorimetric area of LiC_{12} and LiC_6 in the cross-section of battery cells [36]. Even though the colorimetric method has been employed in relevant studies, the limitations of this method when applied to particles in commercial batteries with poor consistency remain unsolved.

In summary, thorough studies on ILIH and its quantitative characterization are crucial for enhancing the durability and safety of LIBs. Nevertheless, to the best of the authors’ knowledge, there have been very few studies that have successfully characterized ILIH during the (dis)charging process, let alone established a quantitative ILIH measuring method.

In this research, an operando optical microscopic approach was used to obtain simultaneous electrical and chromatic image data. Furthermore, a new data analysis method is proposed to characterize the Li intercalation level of anode graphite particles in commercial batteries, enabling the quantitative characterization of ILIH. The robustness of the method was verified via the results obtained from multiple battery cells subjected to different charging and discharging rates. Additionally, based on the relationship between ILIH and the SOC, the electrochemical mechanism underlying the trend of ILIH along the SOC is further discussed.

The remainder of this article is organized as follows: In Section 2, the sample preparation and experimental settings are introduced. In Section 3, the newly proposed ILIH assessment method is detailed, and its necessity is briefly explained through a preliminary analysis of the optical signal. The results of the ILIH assessment are shown in Section 4. Finally, the conclusions and outlooks of this study are provided in Section 5.

2. Experiments

In this section, the experimental details for preparing the battery samples and conducting optical observations are provided. Also, the experimental settings for the operando optical observations are illustrated.

2.1. Preparation of Battery Samples

As introduced in Section 1, the observations in this study focus on commercial batteries, which are unsuitable for optical observation. Consequently, specific battery samples were prepared beforehand. The flow chart of the sample preparation process is shown in Figure 2. For this study, the objects of investigation were pouch cell batteries with lithium-ion phosphate (LFP) as the cathode material and graphite as the anode material. As Figure 2a shows, the batteries were cut with insulated tools. Subsequently, the cathodes, anodes, and separators were peeled off layer-by-layer and cut into specific sizes. Due to the impracticality of performing the heat pressing process inside a glove box, the configuration of the electrodes and separators had to be fixed by other means. Therefore, the pouch cells were designed to be reassembled into the “G-shape” shown in Figure 2b. As Figure 2c shows, electrolyte injection, encapsulation, and the necessary inspections for leak-proofness and capacity maintenance of the pouch cells were conducted. In order to avoid atmospheric interference, the disassembly and reassembly process described above took place in the glovebox filled with argon gas. Finally, three cycles of low-rate charging and discharging were performed on each battery to ensure the electrical reliability of the battery sample for subsequent observation.

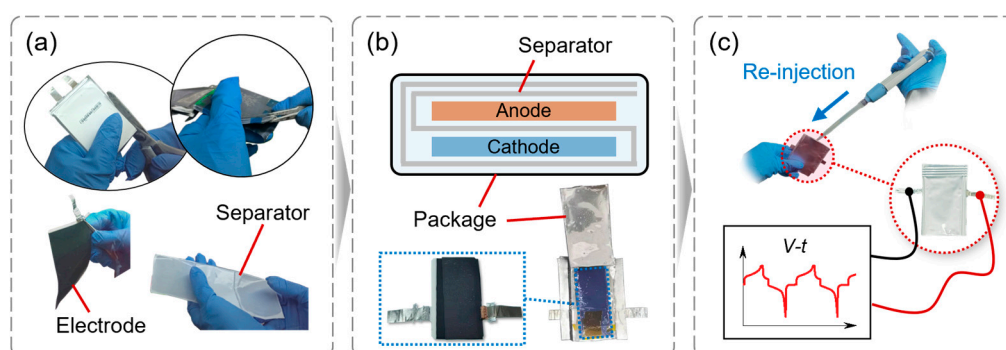


Figure 2. Flow chart of the sample preparation process based on the commercial pouch cell battery: (a) decomposition of the commercial pouch cell battery; (b) reassembly of the single-piece electrode pair pouch cell battery sample; and (c) re-injection of the electrolyte, encapsulation of the battery sample package, and electrical reliability testing of the battery sample.

The cathodes and anodes were cut into sizes of 25 mm × 30 mm and 30 mm × 35 mm, respectively. The samples had an approximate capacity of 20 mAh, with a cut-off voltage range from 2.5 V to 3.65 V.

The optical observation was conducted using the battery sample prepared as described in Figure 2. The operando observation was carried out in a confocal optical microscope (Lasertec Corp., Yokohama, Tokyo, ECCS). The cross-section of the prepared battery sample was continuously illuminated by an independent light source from the microscope, and the reflected light was used to generate confocal chromatic images. The schematic diagram of the sample's cross-section is shown in Figure 2b.

To obtain a high-quality cross-section, the pouch cell sample was cut using a special cutter. The cross-section of the sample was exposed in an anhydrous air environment to protect the electrolytes. Subsequently, the sample was installed in a specially designed airtight fixture. The anhydrous air environment inside the fixture was then replaced with argon gas via a vacuum pump. The exposed cross-section was utilized for the following observations. The operation mentioned above (shown in Figure 3) was vital for maintaining the chemical stability of the exposed battery throughout long-term testing.

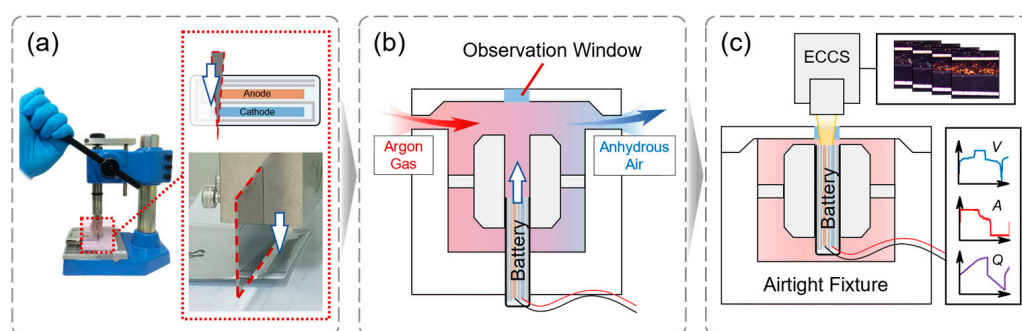


Figure 3. Flow chart of the optical observation based on confocal optical microscopy: (a) exposure of the cross-section of the sample; (b) schematic of sample installation and the gas replacement process; and (c) schematic of optical observation.

2.2. Experimental Settings

In this article, the experiments were conducted at room temperature (25 °C). The confocal microscope was utilized for the operando observation, enabling the acquisition of a series of high-resolution photochromes synchronized with the electrical data in the (dis)charging process.

The following protocol was adopted for this study: (1) constant current (CC) charging to 3.65V at 1/8C and then constant voltage (CV) charging at 3.65 V until the current is reduced to 1/20C; (2) rest for 5 min; (3) CC discharging to 2.5 V at 1/8C; (4) rest for 5 min; (5) repeat steps (1) through (4) three times, changing the CC charging and discharging rate to 1/4C, 1/2C, and 1C.

As discussed in Section 1, inhomogeneous Li intercalation occurs during high-rate charging/discharging processes, whereas the inhomogeneity in slow charging/discharging processes can be neglected. Therefore, for the sake of comparison, low-rate charging/discharging (1/8C) was set as the homogeneous baseline. Further discussions and hypotheses are introduced in the following analysis.

3. Methods

Based on the optical and electrical data obtained in the experiments, a series of data analysis processes were conducted. The corresponding methods are fully illustrated in this section. The section begins by presenting an intuitive analysis of the optical signal from the cross-sections of the batteries, highlighting the necessity of the ILIH assessment method, which is further introduced in this section.

3.1. Preliminary Analysis of the Optical Signal

In this subsection, we illustrate that the color response of the cross-sections on the anode side is highly sensitive to changes in battery SOC, and significant inhomogeneity in the intra-layer direction can be observed. However, owing to the inherent randomness of commercial batteries, the statistical results exhibit the limitation of the colorimetric method in identifying the SOCs of local regions and characterizing the ILIH values.

In this study, three battery samples were tested and observed. One sample was selected to demonstrate the characteristics of the operando optical response. Figure 4 presents the representative electrical signal of the battery in the tests, whereas Figure 5a illustrates the color reaction of the graphite lithiation process captured by optical microscopy. As the lithiation process progresses, the Lithium–Carbon composite in the anode undergoes a color change reaction, transitioning from grey to blue, orange, and gold [35,36]. This physicochemical phenomenon is a consequence of the transition between different phases within the Lithium–Carbon composite during lithiation and delithiation processes, which can be readily discerned through optical observation. At room temperature, the phases correspond to $\text{Li}_{0.04}\text{C}_6$ - $\text{Li}_{0.33}\text{C}_6$ - $\text{Li}_{0.5}\text{C}_6$ - LiC_6 , correlating with a color transition from grey to dark blue to orange (or dark red) to gold [22,37]. Moreover, distinctive differences in the graphite color in the cross-section were observed at different charging rates. The arrows in Figure 5a indicate that higher charging rates result in a larger golden area near the separator and a larger blue area further away from the separator, which can be classified as an ILIH phenomenon. On the other hand, previous studies [23] and the observations in Figure 5a indicate that the LFP cathode material exhibited insignificant optical variation throughout the lithiation and delithiation processes. Additionally, variations in the size and distribution of anode graphite particles were observed in commercial battery coatings, primarily due to the manufacturing process.

In previous studies, the colorimetric method has been employed to determine the SOC of the particles. However, due to the inherent randomness resulting from the experimental settings, sample preparation, anode material systems, etc., the colorimetric method was not suitable for evaluating the Li intercalation status of the local area of interest.

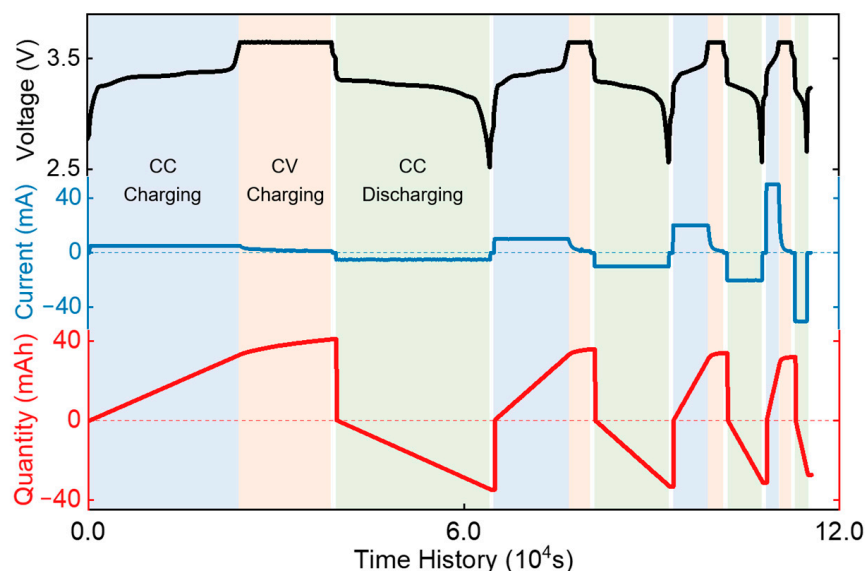


Figure 4. Original voltage–current–time data and the calculated electric charge quantity (to demonstrate the data clearly, the electric charge quantity value in the discharging process was set as negative, so the absolute value represents the battery’s discharge capability).

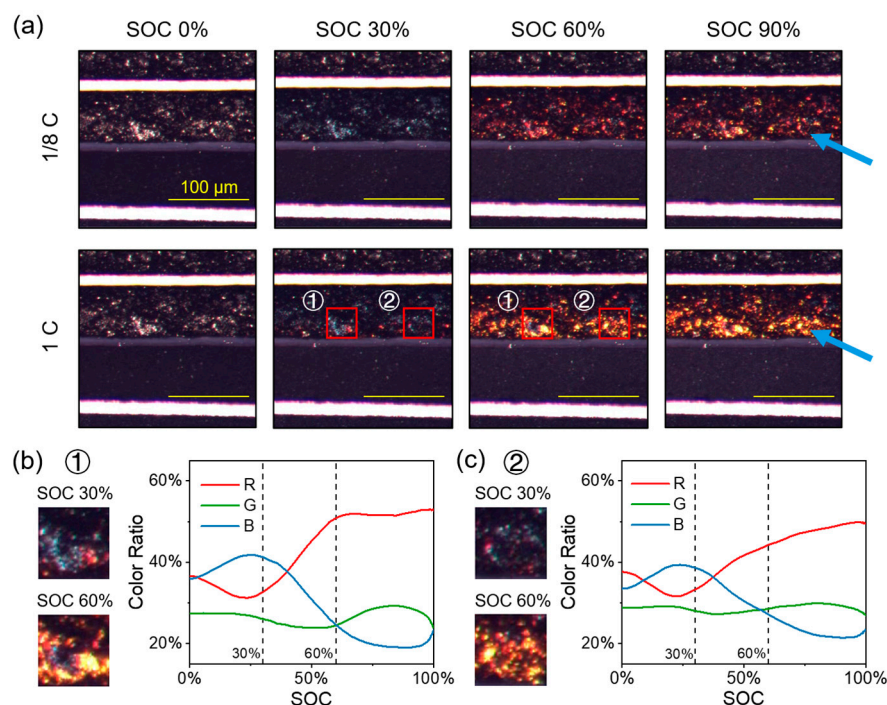


Figure 5. The image capture and preliminary analysis results: (a) operando in situ image captures of the cross-sections with different SOCs and charging rates (The blue arrows emphasize the noticeable inhomogeneity at higher charging rates); (b) primary color ratio analysis of part ①; and (c) primary color ratio analysis of part ②.

The primary color ratio analysis in two parts of the same battery sample is shown in Figure 5. The local image captures of part ① and ② (Figure 5a) at 30% SOC and 60% SOC are respectively zoomed in and shown in Figure 5b,c. The primary color ratios of these two parts were calculated throughout the 0.125C charging process, and the results are presented in curve graphs. In these graphs, the short-dashed lines indicate the positions of 30% and 60% SOC. The inconsistent color ratio trends of the primary colors indicate variations in the color reaction at different local areas. The differences between part ① and ② are also obvious intuitively: at the same 30% SOC condition, they exhibit a similar blueish color, whereas at the same 60% SOC condition, the particles in part ② turn orange to a similar extent. Furthermore, in part ①, some particles become bright gold, whereas others remain blue.

From the preliminary analysis, it is evident that there are variations in the color change among different parts of the cross-section. Therefore, a single absolute criterion is not suitable for quantitatively analyzing the intricate information obtained from the image. This introduces non-negligible interference in the absolute colorimetric analysis process and may bring limitations to the existing colorimetric methods. Hence, in order to evaluate the real-time ILIH value of the battery, a new method is introduced (in the following section).

3.2. ILIH Assessment Method

In this subsection, the ILIH assessment method is explained in detail. The method was based on the color change of the Lithium–Carbon composite in the anode during its Li intercalation: a grey–blue–red–gold color reaction along with the intercalation reaction of $\text{Li}_{0.04}\text{C}_6$ – $\text{Li}_{0.33}\text{C}_6$ – $\text{Li}_{0.5}\text{C}_6$ – LiC_6 [35–37]. However, to overcome the inherent randomness mentioned above, the assessment could not rely on absolute criteria. Therefore, this paper has established a relative criterion using the optical data obtained during low-rate (dis)charging processes. Through a series of data processing operations, the quantitative assessment of ILIH was achieved.

Specifically, the data processing operations included: characterization of the Original Relative Illuminance, which managed to normalize the data in a positional sense, as introduced in Section 3.2.1; calculation of the Normalized Relative Illuminance, which normalizes the data in terms of illuminance, as introduced in Section 3.2.2; and characterization of the ILIH value, which included a linear simplification process and an angular decomposition process aimed at eliminating systematic inhomogeneity noise, as introduced in Section 3.2.3.

3.2.1. Characterization of the Original Relative Illuminance

As mentioned before, the randomness in battery electrode manufacturing leads to different sizes and non-uniform distribution of the anode graphite particles. Moreover, the thickness and position of the electrode coating also changes during charging and discharging processes, which can be seen in Supplementary Video S1. This is mainly due to the volume change of electrode particles in the (de)lithiation process and other environmental disturbances. Thus, the absolute position of the anode coating (the object of this study) cannot be guaranteed.

In order to carry out an operando comparison of the same sample under different SOCs, charging rates, battery cells, etc., it is necessary to eliminate the influence of component deformation and position shifting on image data. As a result, to obtain robust quantitative results from the image analysis of the battery samples, the following operation is required.

The Original Relative Illuminance (ORI) is calculated by analyzing the color information of the photochrome captured in optical microscopy. Figure 6a shows a typical part of the image capture when Battery-A (one of the studied battery samples) was fully charged. In this image, ①④⑥ represent the anode and ②⑤⑦ represent the cathode. Only ④①②③⑤ and the external circuit form a complete loop.

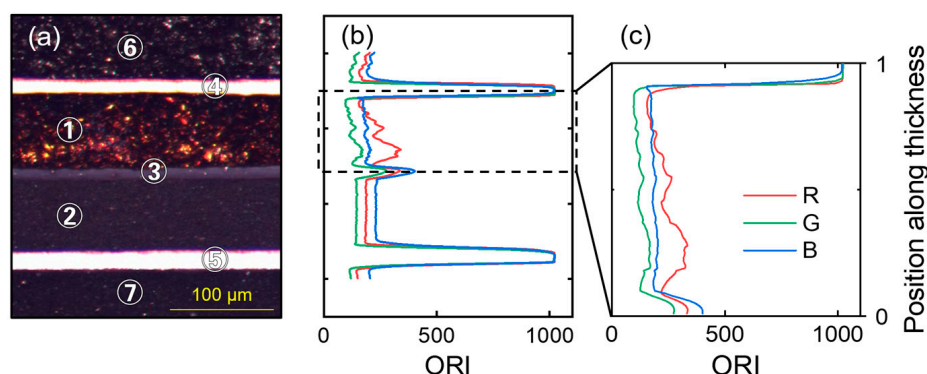


Figure 6. Data analyzing process of ORI: (a) Original image capture in ECCS: ① Anode Coating (in loop); ② Cathode Coating (in loop); ③ Separator; ④ Anode Current Collector (Cu); ⑤ Cathode Current Collector (Al); ⑥ Anode Coating (out of loop); and ⑦ Cathode Coating (out of loop); (b) ORI directly extracted from the original image capture; (c) the result of position normalization for the ORI.

Figure 6b presents the ORI extracted from the original image (Figure 6a) by summing up the primary color values of pixels on the same row (perpendicular to the anode coating thickness direction). The upper and lower boundaries of the anode coating were identified according to the optical characteristics of the separator (③) and current collector (④), respectively. Then, the pixels boxed in the identified area were isolated and characterized in terms of their relative position (ranging from 0 to 1) along the anode coating thickness direction.

Figure 6c shows the result of position normalization for the ORI. This process helps to eliminate interference caused by the volume change of the battery or any wobbling of the microscope.

3.2.2. Calculation of the Normalized Relative Illuminance

As mentioned earlier, non-uniformity in graphite particle size, distribution, and physicochemical characteristics can arise due to experimental settings, sample preparation, the manufacture of anode coatings, anode material systems, etc. Non-uniformity may cause inconsistent color reactions and incomparable illuminance changes, posing challenges in evaluating the Li intercalation status of the local area of interest.

In order to address the challenges posed by the inherent randomness mentioned above, this article proposed a method: normalizing the ORI of one of the primary colors to establish consistent “Color–Li intercalation” relationships across different local areas. The normalized ORI is referred to as the Normalized Relative Illuminance (NRI) throughout the rest of this article.

The formula for calculating NRI is as follows:

$$\text{NRI}(x, t; \text{Color}) = \frac{\text{ORI}(x, t; \text{Color}) - \min_t \text{ORI}(x, t; \text{Color})}{\max_t \text{ORI}(x, t; \text{Color}) - \min_t \text{ORI}(x, t; \text{Color})} \quad (1)$$

where, x is the relative position along the thickness in the anode coating (ranging from 0 to 1); t denotes the time history; Color represents the RGB primary colors. Using the formula, the minimum and maximum values of ORI were calculated at each x_0 point with respect to t . Consequently, NRI serves as a rational characterization parameter for the Relative Lithium Insertion Amount (RLI) of the anode. Figure 7 illustrates the calculation process of $\text{NRI}(x, t; \text{Red})$, wherein the following equations are satisfied:

$$\text{ORI}_{\min}(x) = \text{ORI}(x, t_{\min}; \text{Red}) = \min_t \text{ORI}(x, t; \text{Red}), \quad (2)$$

$$\text{ORI}_{\max}(x) = \text{ORI}(x, t_{\max}; \text{Red}) = \max_t \text{ORI}(x, t; \text{Red}), \quad (3)$$

where any $x_0 \in [0, 1]$.

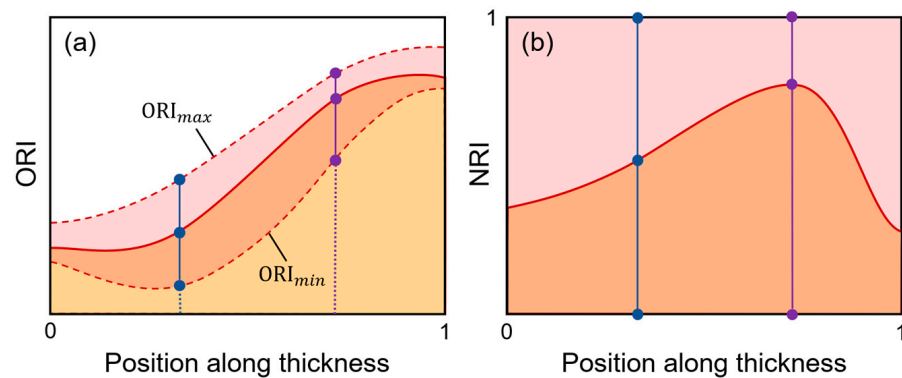


Figure 7. Schematic diagram of the NRI calculation process (the blue and purple vertical lines in the two subplots have the same proportions): (a) an ORI curve at time t (solid line), and the maximum and minimum curves of $\text{ORI}(x, t_{\max}; \text{Red})$ and $\text{ORI}(x, t_{\min}; \text{Red})$; and (b) the NRI curve derived from (a).

By normalizing the local illuminance of ORI, the inherent difference among the particles at different relative positions can be reduced to an acceptable extent. As a result, real-time evaluation of ILIH in the battery sample can be further achieved using NRI data.

3.2.3. Characterization of the Intra-Layer Inhomogeneity (ILIH) Value

The ILIH is specifically represented by the degree of SOC deviation at different positions along the thickness direction. In this study, the authors tried to describe ILIH with a specific “ILIH value”, represented by K_{ILIH} . In the practical analysis process, the determination of this slope is based on the fitting of NRI at different positions along the thickness direction. However, it should be emphasized that the NRI value at a particular

location cannot directly represent the local SOC. As mentioned before, the manufacturing of commercial batteries and the preparation of samples in the laboratory may introduce systematic deviations to the relationship between NRI and SOC. To overcome this deviation, K_{ILIH} during low-rate (dis)charging processes (1/8C in this case) is considered zero, i.e., it is considered homogeneous. Consequently, the NRI slope values in the low-rate process represent the systematic noise of the sample at specific SOC. Therefore, the following operation is required to eliminate systematic deviations and to obtain the assessed ILIH value (K_{ILIH}).

Figure 8 presents the schematic diagrams related to NRI fitting and the ILIH characterization process. Time t_1 corresponds to medium/high-rate conditions (1/4C, 1/2C, or 1C in this case), whereas time t_0 corresponds to low-rate conditions (1/8C in this case). Notably, the battery sample is at the same SOC at both moments. As mentioned before, K_{ILIH} in low-rate conditions is considered systematic noise. So, as Figure 8a illustrates, a comparison between t_1 and t_0 can derive K_{ILIH} with a specified SOC and charging/discharging rate.

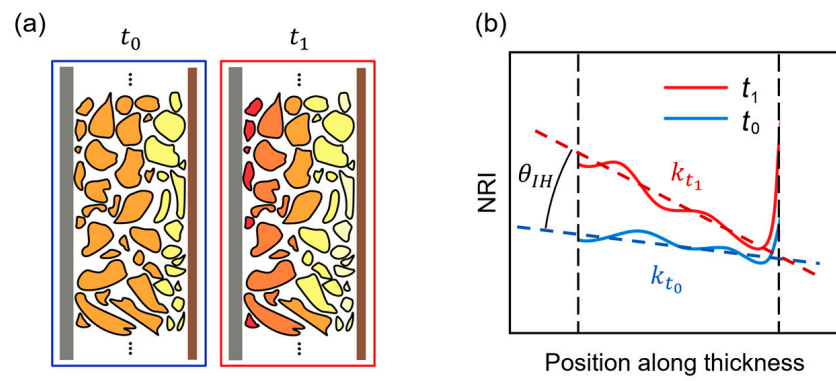


Figure 8. Schematic diagrams related to the characterization of K_{ILIH} . (a) Schematic diagram of the original inhomogeneity noise in the slow charging process when $SOC(t_0) = SOC(t_1)$, $K_{ILIH}(t_0) \equiv 0$; and (b) schematic diagram of the NRI fitting process.

Figure 8b illustrates the NRI fitting process, in which the estimation of K_{ILIH} is made. Systematic noise needs to be excluded from the image analysis results at t_1 , so an angular decomposition formula was derived as follows:

$$\tan(\theta_{k_{t_0}}) = k_{t_0} \tag{4}$$

$$\tan(\theta_{k_{t_1}}) = k_{t_1} \tag{5}$$

$$SOC(t_0) = SOC(t_1) \tag{6}$$

$$K_{ILIH}(t_1) := \tan \theta_{IH} = \tan(\theta_{k_{t_1}} - \theta_{k_{t_0}}) = \frac{k_{t_1} - k_{t_0}}{1 + k_{t_1}k_{t_0}} \tag{7}$$

in which case, as t_0 is in the low-rate charging process, $K_{ILIH}(t_0)$ is considered to be zero.

To summarize, the ILIH value assessment process is outlined in a flow chart, as shown in Figure 9. The nominalization of position and illuminance ensures reliability at both the position and color levels, respectively. This process converts the qualitative and unstable image results into quantitative and robust K_{ILIH} results.

Significantly, because the images, ORI, NRI, and K_{ILIH} are time series data, a data-navigating video can be generated during processing. Furthermore, the data-navigating video can assist in error checking during the data analysis process. An example of a data-navigating video is provided in Supplementary Video S2, and a brief introduction and analysis of the video can be found in the Supplementary Material. A detailed analysis of the K_{ILIH} results will be discussed in the next section.

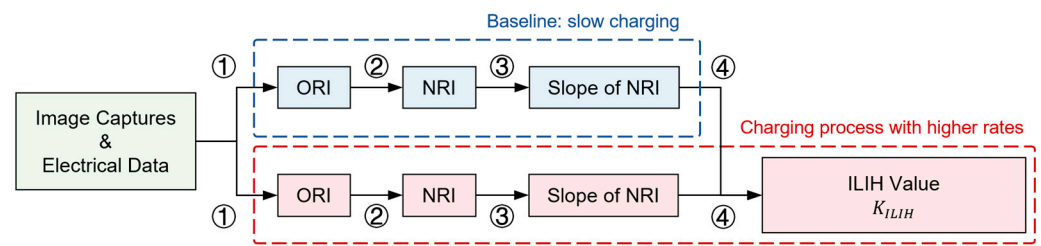


Figure 9. Flow chart of the ILIH assessment process: ① nominalization of position; ② nominalization of illuminance; ③ linear simplification; and ④ elimination of inhomogeneity noise.

4. Results and Discussions

By applying the ILIH assessment method demonstrated above, a series of K_{ILIH} results were obtained, all of which are illustrated and discussed in this section. In Section 4.1, the K_{ILIH} results are presented and discussed, and the robustness of the introduced method is verified for different battery samples with different charging rates. In Section 4.2, the K_{ILIH} trend and its underlying physicochemical mechanism are illustrated and discussed in detail, providing support to the interpretability of the ILIH assessment method.

4.1. Results of ILIH Value Assessment

As shown in Figure 5 and Supplementary Video S2, the Red Channel exhibits the most significant changes during the (dis)charging process. Therefore, processing the Red Channel data would be highly beneficial in characterizing ILIH. Consequently, a series of K_{ILIH} -SOC data (via the Red Channel) from different batteries and charge/discharge rates are sorted out.

Figure 10 illustrates the K_{ILIH} -SOC plot during the charging process of the three batteries, whereas Figure 11 shows the plot during the discharging process. Due to slight electrochemical instability in Battery-C, the charging/discharging rates did not precisely match the pre-set values in the tests, and the 1C rate was not properly executed. However, because the three cycles were still comparable (0.172C is close to 0.125C, and 0.345C and 0.69C are two times and four times the 0.172C baseline), Battery-C was still worth analyzing. For the sake of clarity, the three different charging rates are uniformly expressed as “0.125C”, “0.25C”, and “0.5C” throughout this study. Additionally, the cross-section of the Battery-B sample exhibited lower reflectance in the ECCS, resulting in dimmer original photochromatic captures that were more easily affected by systematic noise, leading to greater fluctuations in its K_{ILIH} -SOC plot.

In the charging process, K_{ILIH} has negative values because the zero point of position along the thickness is defined on the separator side. It is important to note that the positive and negative values of K_{ILIH} represent the direction of inhomogeneity, whereas the absolute value refers to the extent of inhomogeneity. Figure 10 shows a similar K_{ILIH} trend, including a near-zero plateau at low SOCs, a rapid change at medium-high SOCs, and restoration at high SOCs.

During the discharging process, shown in Figure 11, K_{ILIH} returns to zero as the SOC decreases. Battery-A and Battery-B exhibit similar trends, whereas Battery-C behaves differently, with barely any change in K_{ILIH} during the discharging process. The divergent trend is attributed to the different end points of K_{ILIH} -SOC in the charging process, where Battery-C has large positive end points instead of negative ones. In the experiments, Battery-C undergoes an extremely short CV charging process compared to Battery-A and Battery-B, which may result in abnormal charging end points. The authors believe that the abnormal behavior of Battery-C in this case may also result from the sample’s slight electrochemical instability.

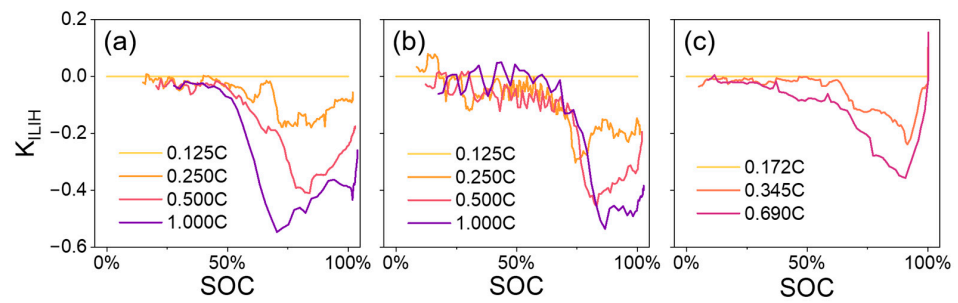


Figure 10. K_{ILIH} -SOC plot of the charging process: (a) Battery-A; (b) Battery-B; and (c) Battery-C.

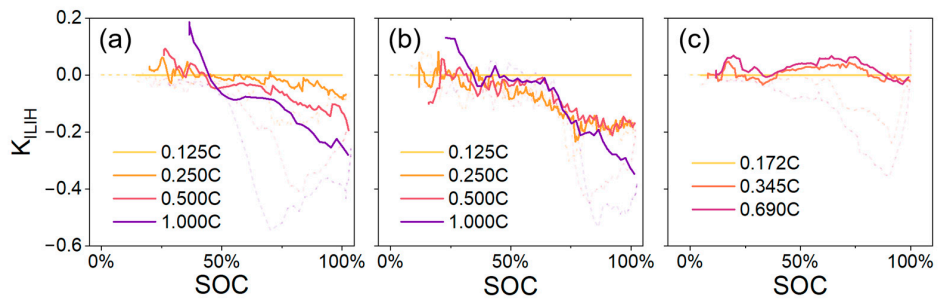


Figure 11. K_{ILIH} -SOC plot of the discharging process: (a) Battery-A; (b) Battery-B; and (c) Battery-C.

By combining the K_{ILIH} -SOC curves obtained at the same charging rates, as shown in Figure 12a–c, a comparison between different battery cells can be made. The peak K_{ILIH} (in the negative domain) was -0.24 ± 0.06 at 0.25C and -0.41 ± 0.05 at 0.5C, whereas in the 1C condition (excluding Battery-C), the peak value was approximately -0.55 . The peak K_{ILIH} results are summarized in Figure 12d. The relationship exhibits an increasing trend with increasing charging rate. In conclusion, the quantitative ILIH characterization method demonstrates robustness across different battery cells and charging rates.

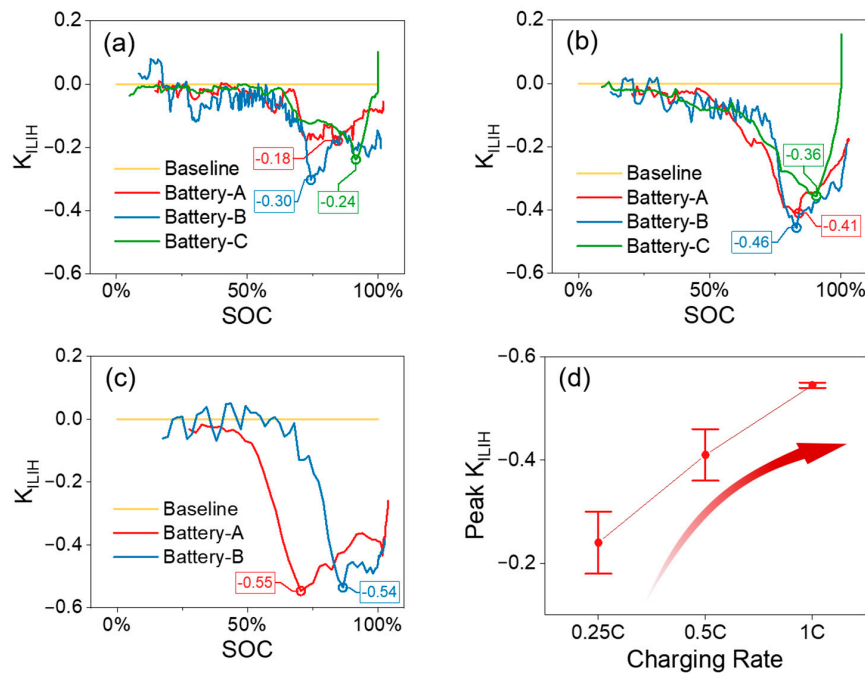


Figure 12. Results of peak K_{ILIH} in the charging process: (a) K_{ILIH} at 1/4C charging rate; (b) K_{ILIH} at 1/2C charging rate; (c) K_{ILIH} at 1C charging rate; and (d) the relationship between peak K_{ILIH} and the charging rates.

4.2. ILIH Value Trend Analysis

To provide a detailed analysis of the charging K_{ILIH} -SOC curve trend, a specific curve is singled out in Figure 13. By focusing on the 0.5C single CC-CV-CC cycle of Battery-A as an example, the K_{ILIH} -SOC curve can be divided into six parts. For each part, a Relative Lithium Insertion Amount vs. Position graph is shown in Figure 13 to illustrate the underlying mechanism. The Relative Lithium Insertion Amount (RLI) represents the relative insertion amount at each position along the thickness based on the assessment approach proposed in this study. It is important to note that the rectangular dashed frame in Figure 13 represents the fully charged status in the real-world low-rate charging process, which is not equivalent to the theoretical fully inserted state of Li.

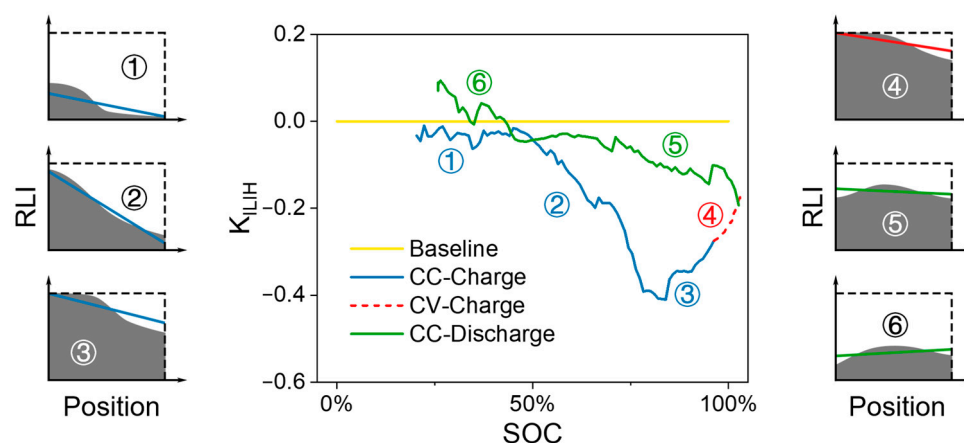


Figure 13. K_{ILIH} -SOC plot from the experiment of Battery-A, with a 0.5C charging process, and Relative Lithium Insertion Amount (RLI) vs. Position schematic diagrams are shown from the concept.

The six parts and the underlying mechanism are as follows:

①: Only anode particles near the separator start Li insertion, but because the fitting of NRI covers the entire anode, K_{ILIH} (or the fitted NRI slope) changes minimally.

②: Li inserts into particles evenly, resulting in a rapid change in K_{ILIH} towards a significant negative value within a narrow SOC range.

③: Anode particles near the separator reach the maximum insertion amount, whereas the insertion of particles near the current collector continues, causing K_{ILIH} to decrease.

④: In the CV charging process, K_{ILIH} continues to decrease.

⑤ and ⑥: In the CC discharging process, Li begins to take off from the separator side particle. So, K_{ILIH} decreases in the negative domain until it reaches zero, and then it continues to increase.

Based on the underlying mechanism, it becomes evident that enhancing anode materials and refining the manufacturing process through parameter optimization, such as microstructure and material system adjustments, may elevate the diffusion rate within the anode coating layer. These improvements hold the promise of mitigating ILIH during the reaction process and, consequently, improving the stability of fast-charging battery systems.

Although no literature strictly supports the mechanism of the demonstrated K_{ILIH} -SOC trend, the mechanism proposed in this paper was inspired by Guo et al. [38] and Krachkovskiy et al. [32]. Nevertheless, the K_{ILIH} trend and its underlying mechanism effectively support the interpretability of the ILIH assessment method.

5. Conclusions and Outlooks

5.1. Conclusions

This study successfully conducted an operando observation and characterization of the cross-section of commercial battery anodes. The newly introduced analysis method enables the quantification of intra-layer inhomogeneity in operating cells. A detailed analysis of the relationship between the ILIH value (K_{ILIH}) and SOC was performed. The

peak inhomogeneity values between different cells and charging rates exhibit a great degree of convergence. Thus, the new method has been demonstrated to be robust in different conditions and overcomes the limitations of the colorimetric method.

5.2. Outlooks

The proposed method holds great potential for future studies, with the following possibilities:

- (1) Adoption of the new method for graphite anodes (or various cathodes) in various battery material systems.
- (2) Conducting large-scale factorial experiments to establish functional relationships between the trend of ILIH values, SOCs, charging rates, and the current ILIH value. Then, the relationship functions can be used as guidance for setting fast charging protocols. The newly guided protocols may result in a longer lifespan and better health conditions of commercial batteries compared to protocols solely scaled from Li plating limits.
- (3) By combining the new method for characterizing ILIH with Digital Image Correlation (DIC) techniques for electrode strain measurement, the relationships between strain and Li intercalation inhomogeneity can be studied extensively. Furthermore, by using nanoindentation to measure the mechanical properties of particles and other materials in the cross-section, an inner stress study can be conducted to further elucidate the relationships between particle cracking, stress (or strain) distribution, and the inhomogeneity of Li intercalation.

Supplementary Materials: The following supporting information can be downloaded at: <https://www.mdpi.com/article/10.3390/batteries9090463/s1>.

Author Contributions: Conceptualization, P.Y.; methodology, T.F. and P.Y.; software, T.F. and P.Y.; validation, T.F. and P.Y.; formal analysis, T.F. and P.Y.; investigation, T.F. and G.J.; resources, G.J.; data curation, G.J.; writing—original draft preparation, T.F.; writing—review and editing, Y.X. and P.Y.; visualization, T.F.; supervision, Y.X. and P.Y.; project administration, P.Y.; funding acquisition, Y.X. All authors have read and agreed to the published version of the manuscript.

Funding: This study was sponsored by the National Natural Science Foundation of China (Grant No. 52172405). This study was also partially supported by the University Research Program of Ford (Grant No. 001068-2019-7170R-H).

Data Availability Statement: The data presented in this study are available on request from the corresponding author. The data are not publicly available due to confidentiality reasons.

Conflicts of Interest: The authors declare no conflict of interest.

References

1. Whittingham, M.S. Lithium Batteries and Cathode Materials. *Chem. Rev.* **2004**, *104*, 4271–4302. [[CrossRef](#)] [[PubMed](#)]
2. Duan, J.; Tang, X.; Dai, H.; Yang, Y.; Wu, W.; Wei, X.; Huang, Y. Building Safe Lithium-Ion Batteries for Electric Vehicles: A Review. *Electrochem. Energ. Rev.* **2020**, *3*, 1–42. [[CrossRef](#)]
3. Kim, T.; Song, W.; Son, D.-Y.; Ono, L.K.; Qi, Y. Lithium-Ion Batteries: Outlook on Present, Future, and Hybridized Technologies. *J. Mater. Chem. A* **2019**, *7*, 2942–2964. [[CrossRef](#)]
4. Li, W.; Erickson, E.M.; Manthiram, A. High-Nickel Layered Oxide Cathodes for Lithium-Based Automotive Batteries. *Nat. Energy* **2020**, *5*, 26–34. [[CrossRef](#)]
5. Zeng, X.; Li, M.; Abd El-Hady, D.; Alshitari, W.; Al-Bogami, A.S.; Lu, J.; Amine, K. Commercialization of Lithium Battery Technologies for Electric Vehicles. *Adv. Energy Mater.* **2019**, *9*, 1900161. [[CrossRef](#)]
6. Pang, P.; Wang, Z.; Deng, Y.; Nan, J.; Xing, Z.; Li, H. Delayed Phase Transition and Improved Cycling/Thermal Stability by Spinel LiNi_{0.5}Mn_{1.5}O₄ Modification for LiCoO₂ Cathode at High Voltages. *ACS Appl. Mater. Interfaces* **2020**, *12*, 27339–27349. [[CrossRef](#)]
7. Pang, P.; Wang, Z.; Tan, X.; Deng, Y.; Nan, J.; Xing, Z.; Li, H. LiCoO₂@LiNi_{0.45}Al_{0.05}Mn_{0.5}O₂ as High-Voltage Lithium-Ion Battery Cathode Materials with Improved Cycling Performance and Thermal Stability. *Electrochim. Acta* **2019**, *327*, 135018. [[CrossRef](#)]
8. Nitta, N.; Wu, F.; Lee, J.T.; Yushin, G. Li-Ion Battery Materials: Present and Future. *Mater. Today* **2015**, *18*, 252–264. [[CrossRef](#)]
9. Waldmann, T.; Hogg, B.-I.; Wohlfahrt-Mehrens, M. Li Plating as Unwanted Side Reaction in Commercial Li-Ion Cells—A Review. *J. Power Sources* **2018**, *384*, 107–124. [[CrossRef](#)]

10. Harris, S.J.; Lu, P. Effects of Inhomogeneities—Nanoscale to Mesoscale—On the Durability of Li-Ion Batteries. *J. Phys. Chem. C* **2013**, *117*, 6481–6492. [[CrossRef](#)]
11. Sasaki, T.; Villevieille, C.; Takeuchi, Y.; Novák, P. Understanding Inhomogeneous Reactions in Li-Ion Batteries: Operando Synchrotron X-Ray Diffraction on Two-Layer Electrodes. *Adv. Sci.* **2015**, *2*, 1500083. [[CrossRef](#)] [[PubMed](#)]
12. Nakamura, T.; Watanabe, T.; Kimura, Y.; Amezawa, K.; Nitta, K.; Tanida, H.; Ohara, K.; Uchimoto, Y.; Ogumi, Z. Visualization of Inhomogeneous Reaction Distribution in the Model LiCoO₂ Composite Electrode of Lithium Ion Batteries. *J. Phys. Chem. C* **2017**, *121*, 2118–2124. [[CrossRef](#)]
13. He, J.; Meng, J.; Huang, Y. Challenges and Recent Progress in Fast-Charging Lithium-Ion Battery Materials. *J. Power Sources* **2023**, *570*, 232965. [[CrossRef](#)]
14. Huang, Q.; Ni, S.; Jiao, M.; Zhong, X.; Zhou, G.; Cheng, H.-M. Aligned Carbon-Based Electrodes for Fast-Charging Batteries: A Review. *Small* **2021**, *17*, 2007676. [[CrossRef](#)]
15. Yari, S.; Van Bael, M.K.; Hardy, A.; Safari, M. Non-Uniform Distribution of Current in Plane of Large-Area Lithium Electrodes. *Batter. Supercaps* **2022**, *5*, e202200217. [[CrossRef](#)]
16. Zhu, X.; Revilla, R.I.; Jaguemont, J.; Van Mierlo, J.; Hubin, A. Insights into Cycling Aging of LiNi_{0.80}Co_{0.15}Al_{0.05}O₂ Cathode Induced by Surface Inhomogeneity: A Post-Mortem Analysis. *J. Phys. Chem. C* **2019**, *123*, 30046–30058. [[CrossRef](#)]
17. Mühlbauer, M.J.; Schökel, A.; Etter, M.; Baran, V.; Senyshyn, A. Probing Chemical Heterogeneity of Li-Ion Batteries by in Operando High Energy X-Ray Diffraction Radiography. *J. Power Sources* **2018**, *403*, 49–55. [[CrossRef](#)]
18. Maire, P.; Kaiser, H.; Scheifele, W.; Novák, P. Colorimetric Determination of Lithium-Ion Mobility in Graphite Composite Electrodes. *J. Electroanal. Chem.* **2010**, *644*, 127–131. [[CrossRef](#)]
19. Vamvakeros, A.; Matras, D.; Ashton, T.E.; Coelho, A.A.; Dong, H.; Bauer, D.; Odarchenko, Y.; Price, S.W.T.; Butler, K.T.; Gutowski, O.; et al. Cycling Rate-Induced Spatially-Resolved Heterogeneities in Commercial Cylindrical Li-Ion Batteries. *Small Methods* **2021**, *5*, 2100512. [[CrossRef](#)]
20. Petz, D.; Mühlbauer, M.J.; Baran, V.; Schökel, A.; Kochetov, V.; Hofmann, M.; Dyadkin, V.; Staron, P.; Vaughan, G.; Lienert, U.; et al. Lithium Distribution and Transfer in High-Power 18650-Type Li-Ion Cells at Multiple Length Scales. *Energy Storage Mater.* **2021**, *41*, 546–553. [[CrossRef](#)]
21. Senyshyn, A.; Mühlbauer, M.J.; Dolotko, O.; Hofmann, M.; Ehrenberg, H. Homogeneity of Lithium Distribution in Cylinder-Type Li-Ion Batteries. *Sci. Rep.* **2015**, *5*, 18380. [[CrossRef](#)] [[PubMed](#)]
22. Harris, S.J.; Timmons, A.; Baker, D.R.; Monroe, C. Direct In Situ Measurements of Li Transport in Li-Ion Battery Negative Electrodes. *Chem. Phys. Lett.* **2010**, *485*, 265–274. [[CrossRef](#)]
23. Hogrefe, C.; Waldmann, T.; Hölzle, M.; Wohlfahrt-Mehrens, M. Direct Observation of Internal Short Circuits by Lithium Dendrites in Cross-Sectional Lithium-Ion In Situ Full Cells. *J. Power Sources* **2023**, *556*, 232391. [[CrossRef](#)]
24. Kuwabara, J.; Sato, K. In Situ Observation of the Electrochemical Dissolution and Deposition of Copper Contaminations in Li-Ion Batteries. *ECS Trans.* **2017**, *75*, 47. [[CrossRef](#)]
25. Zhu, J.; Zhang, X.; Luo, H.; Sahraei, E. Investigation of the Deformation Mechanisms of Lithium-Ion Battery Components Using in-Situ Micro Tests. *Appl. Energy* **2018**, *224*, 251–266. [[CrossRef](#)]
26. Tian, X.; Ying, P.; Xia, Y. In-Situ Mechanical Characterization of Compression Response of Anode Coating Materials through Inverse Approach. In Proceedings of the SAE 2022 International Automotive Safety, Security and Testing Congress, Shanghai, China, 7–8 July 2022.
27. Paul, P.P.; McShane, E.J.; Colclasure, A.M.; Balsara, N.; Brown, D.E.; Cao, C.; Chen, B.-R.; Chinnam, P.R.; Cui, Y.; Dufek, E.J.; et al. A Review of Existing and Emerging Methods for Lithium Detection and Characterization in Li-Ion and Li-Metal Batteries. *Adv. Energy Mater.* **2021**, *11*, 2100372. [[CrossRef](#)]
28. Meyer, L.; Saqib, N.; Porter, J. Review—Operando Optical Spectroscopy Studies of Batteries. *J. Electrochem. Soc.* **2021**, *168*, 090561. [[CrossRef](#)]
29. Steiger, J.; Kramer, D.; Mönig, R. Mechanisms of Dendritic Growth Investigated by In Situ Light Microscopy during Electrodeposition and Dissolution of Lithium. *J. Power Sources* **2014**, *261*, 112–119. [[CrossRef](#)]
30. Yui, Y.; Hayashi, M.; Nakamura, J. In Situ Microscopic Observation of Sodium Deposition/Dissolution on Sodium Electrode. *Sci. Rep.* **2016**, *6*, 22406. [[CrossRef](#)]
31. Schweikert, N.; Hofmann, A.; Schulz, M.; Scheuermann, M.; Boles, S.T.; Hanemann, T.; Hahn, H.; Indris, S. Suppressed Lithium Dendrite Growth in Lithium Batteries Using Ionic Liquid Electrolytes: Investigation by Electrochemical Impedance Spectroscopy, Scanning Electron Microscopy, and In Situ ⁷Li Nuclear Magnetic Resonance Spectroscopy. *J. Power Sources* **2013**, *228*, 237–243. [[CrossRef](#)]
32. Krachkovskiy, S.A.; Foster, J.M.; Bazak, J.D.; Balcom, B.J.; Goward, G.R. Operando Mapping of Li Concentration Profiles and Phase Transformations in Graphite Electrodes by Magnetic Resonance Imaging and Nuclear Magnetic Resonance Spectroscopy. *J. Phys. Chem. C* **2018**, *122*, 21784–21791. [[CrossRef](#)]
33. Agrawal, S.; Bai, P. Operando Electrochemical Kinetics in Particulate Porous Electrodes by Quantifying the Mesoscale Spatiotemporal Heterogeneities. *Adv. Energy Mater.* **2021**, *11*, 2003344. [[CrossRef](#)]
34. Guo, Z.; Zhu, J.; Feng, J.; Du, S. Direct In Situ Observation and Explanation of Lithium Dendrite of Commercial Graphite Electrodes. *RSC Adv.* **2015**, *5*, 69514–69521. [[CrossRef](#)]

35. Maire, P.; Evans, A.; Kaiser, H.; Scheifele, W.; Novák, P. Colorimetric Determination of Lithium Content in Electrodes of Lithium-Ion Batteries. *J. Electrochem. Soc.* **2008**, *155*, A862. [[CrossRef](#)]
36. Hogrefe, C.; Waldmann, T.; Molinero, M.B.; Wildner, L.; Axmann, P.; Wohlfahrt-Mehrens, M. Cross-Sectional In Situ Optical Microscopy with Simultaneous Electrochemical Measurements for Lithium-Ion Full Cells. *J. Electrochem. Soc.* **2022**, *169*, 050519. [[CrossRef](#)]
37. Dahn, J.R. Phase Diagram of $\text{Li} \times \text{C}_6$. *Phys. Rev. B* **1991**, *44*, 9170–9177. [[CrossRef](#)] [[PubMed](#)]
38. Guo, Y.; Smith, R.B.; Yu, Z.; Efetov, D.K.; Wang, J.; Kim, P.; Bazant, M.Z.; Brus, L.E. Li Intercalation into Graphite: Direct Optical Imaging and Cahn–Hilliard Reaction Dynamics. *J. Phys. Chem. Lett.* **2016**, *7*, 2151–2156. [[CrossRef](#)]

Disclaimer/Publisher’s Note: The statements, opinions and data contained in all publications are solely those of the individual author(s) and contributor(s) and not of MDPI and/or the editor(s). MDPI and/or the editor(s) disclaim responsibility for any injury to people or property resulting from any ideas, methods, instructions or products referred to in the content.